FERMILAB-PUB-10-424-AE

arXiv:1009.0773v1 [astro-ph.CO] 3 Sep 2010

Mid-Infrared Spectroscopy of Two Lensed Star-forming Galaxies

Ross Fadely[1], Sahar S. Allam[2], Andrew J. Baker[1],
Huan Lin[2], Dieter Lutz[3], Alice E. Shapley[4], Min-Su Shin[5],
J. Allyn Smith[6], Michael A. Strauss[7], & Douglas L. Tucker[2]

ABSTRACT

We present low-resolution, rest-frame $\sim 5-12\,\mu$m *Spitzer*/IRS spectra of two lensed $z \sim 2$ UV-bright star-forming galaxies, SDSS J120602.09+514229.5 and SDSS J090122.37+181432.3. Using the magnification boost from lensing, we are able to study the physical properties of these objects in greater detail than is possible for unlensed systems. In both targets, we detect strong PAH emission at 6.2, 7.7, and 11.3 μm, indicating the presence of vigorous star formation. For J1206, we find a steeply rising continuum and significant [S IV] emission, suggesting that a moderately hard radiation field is powering continuum emission from small dust grains. The strength of the [S IV] emission also implies a sub-solar metallicity of $\sim 0.5\,Z_\odot$, confirming published rest-frame optical measurements. In J0901, the PAH lines have large rest-frame equivalent widths ($> 1\,\mu$m) and the continuum rises slowly with wavelength, suggesting that any AGN contribution to $L_{\rm IR}$ is insignificant, in contrast to the implications of optical emission-line diagnostics. Using [O III] line flux as a proxy for AGN strength, we estimate

[1]Department of Physics and Astronomy, Rutgers, the State University of New Jersey, 136 Frelinghuysen Road, Piscataway, NJ 08854-8019; {fadely,ajbaker}@physics.rutgers.edu

[2]Fermi National Accelerator Laboratory, P.O. Box 500, Batavia, IL 60510; {sallam,hlin,dtucker}@fnal.gov

[3]Max-Planck-Institut für extraterrestrische Physik, Postfach 1312, D-85741 Garching, Germany; lutz@mpe.mpg.de

[4]Department of Astronomy, University of California, Los Angeles, 430 Portola Plaza, Los Angeles, CA 90024; aes@astro.ucla.edu

[5]Department of Astronomy, University of Michigan, 500 Church Street, Ann Arbor, MI 48109; msshin@umich.edu

[6]Department of Physics and Astronomy, Austin Peay State University, P.O. Box 4608, Clarksville, Tennessee 37044; smithj@apsu.edu

[7]Department of Astrophysical Sciences, 4 Ivy Lane, Peyton Hall, Princeton University, Princeton, NJ 08544; strauss@astro.princeton.edu

Operated by Fermi Research Alliance, LLC under Contract No. De-AC02-07CH11359 with the United States Department of Energy.

that the AGN in J0901 provides only a small fraction of its mid-infrared continuum flux. By combining the detection of [Ar II] with an upper limit on [Ar III] emission, we infer a metallicity of $\gtrsim 1.3\,Z_{\odot}$. This work highlights the importance of combining rest-frame optical and mid-IR spectroscopy in order to understand the detailed properties of star-forming galaxies at high redshift.

1. Introduction

Rest-frame UV selection offers a prime view into populations of star-forming galaxies at $z > 1.5$. First used to identify $z \sim 3$ galaxies with sharp breaks in their spectral energy distributions due to absorption below the Lyman limit (Steidel et al. 1996), the Lyman break technique has now been modified and extended to both lower and higher redshift (e.g., Steidel et al. 1999; Lehnert & Bremer 2003; Adelberger et al. 2004). Since the development of the technique in the 1990s, thousands of star-forming galaxies have been spectroscopically confirmed at $z \sim 1.5 - 3.5$ (e.g., Steidel et al. 2003; Reddy et al. 2006a), resulting in a revolution in our understanding of galaxy formation and evolution. However, these high-redshift galaxies suffer from a fundamental problem: they are typically small and faint, with $R_{\rm AB} \geq 24\,$mag, making it impossible to carry out detailed studies of individual objects unless they happen to be strongly lensed. In particular, this limitation applies to observations of UV-bright star-forming systems at the long wavelengths that can trace star formation even in highly obscured regions. While stacking analyses of large samples confirm that UV-selected galaxies at $z \sim 2$ have substantial fractions of their bolometric luminosities emerging in the far-infrared, with $\langle L_{\rm IR}/L_{\rm UV}\rangle \simeq 4 - 5$ (Reddy & Steidel 2004; Reddy et al. 2006b, 2010), understanding the parameters of obscured star formation in individual unlensed objects remains out of reach for current facilities.

The first bright lensed Lyman break galaxies, "cB58" (i.e., MS 1512-cB58) and the "Cosmic Eye" (i.e., LBG J213512.73−010143), were discovered serendipitously in the course of a cluster redshift survey (Yee et al. 1996) and a *Hubble Space Telescope* (*HST*) snapshot imaging survey of X-ray-bright clusters (Smail et al. 2007), respectively. Since clusters are rich in strong caustics capable of producing fold arcs (like cB58) and in individual galaxies capable of producing nearly complete Einstein rings (like the Cosmic Eye), the circumstances of these discoveries were not surprising. More recently, however, several teams have begun to exploit the enormous footprint of the Sloan Digital Sky Survey (SDSS) to identify UV-bright high-redshift sources that are lensed by individual galaxies in field or group environments. This enterprise kicked off with the serendipitous discovery of the "8 O'Clock Arc" (Allam et al. 2007) and has now spawned a variety of systematic searches within the SDSS object

catalog that rely on different selection criteria (e.g., Belokurov et al. 2007; Shin et al. 2008; Hennawi et al. 2008). By focusing on luminous red galaxies with multiple blue neighbors, and on close pairs with characteristic lens+arc morphologies, various authors of this paper have now contributed to the discovery of 11 new spectroscopically confirmed lenses at redshifts $0.4 \leq z \leq 2.4$ (Kubo et al. 2009; Lin et al. 2009; Diehl et al. 2009).

In this paper, we present *Spitzer*/IRS spectroscopy of two objects from this new SDSS sample. The first, SDSS J120602.09+514229.5 (a.k.a. the "Clone", hereafter J1206) is a $z = 2.00$ arc discovered by Lin et al. (2009), who determine a lensing magnification $\mathcal{M} = 27 \pm 1$. The second, SDSS J090122.37+181432.3 (hereafter J0901) is a $z = 2.26$ arc discovered by Diehl et al. (2009); preliminary lens modelling implies a magnification ≈ 8 (A. West et al. 2010 in preparation). Both objects are 20–30 times brighter than galaxies at the knee of the $1.9 \leq z \leq 2.7$ rest-UV luminosity function (Reddy et al. 2008); their estimated intrinsic far-IR luminosities make J1206 a luminous infrared galaxy (LIRG; see Section 3.1) and J0901 an ultraluminous infrared galaxy (ULIRG; see Section 3.2). Here we focus on what can be learned about the conditions in the dusty regions of these galaxies from their integrated mid-infrared emission, based on comparisons with local galaxies, assuming that there is minimal differential lensing across the wavelength ranges of our IRS spectra. We defer to future papers analysis of *Spitzer*/IRAC and (for J1206) MIPS imaging of these targets in light of more refined *HST*-based lens models, together with detailed comparisons to the source-plane properties of similar lensed star-forming galaxies (Siana et al. 2008, 2009) and high-redshift systems selected through their dust emission rather than rest-UV colors (e.g., Lutz et al. 2005; Weedman et al. 2006; Valiante et al. 2007; Yan et al. 2007; Pope et al. 2008; Menéndez-Delmestre et al. 2009).

2. Observations and Data Reduction

We used the Infrared Spectrograph (IRS: Houck et al. 2004) on board the *Spitzer Space Telescope* to obtain $14 - 38\,\mu$m spectra of both J1206 and J0901 in the instrument's "long low" mode ($R \sim 57-126$), for which the first (LL1) and second (LL2) orders cover wavelength ranges of $19-38\,\mu$m and $14-21.3\,\mu$m, respectively. In order to ensure optimal signal-to-noise ratios, we followed the recommendations of Teplitz et al. (2007) and mapped the targets at six positions across the slit. Observations of J1206 were taken during *Spitzer* Cycle 4 (PID 40430; PI S. Allam) on 2007 December 19–20, and consisted of 1×6 pointings in LL1 and LL2 for total integration times of 2.1 ks and 2.2 ks, respectively. J0901 was observed on 2009 May 15 during *Spitzer* Cycle 5 (PID 50086; PI S. Allam) using 2×6 pointings in LL1 totaling 2.2 ks and 2.0 ks, and 1×6 pointings in LL1 totaling 2.2 ks. Data were obtained

under nominal operating conditions, with the exception of the second LL1 Astronomical Observation Request (AOR) for J0901. During this AOR, *Spitzer* began to warm up due to the depletion of its cryogen. The increased thermal background was marginal, raising data collection event (DCE) values by only 6%. The IRS support team deemed the data nominal, and we reduced them following the same procedures used for our other AORs.

Data reduction relied on standard analysis packages and followed the procedure described by Teplitz et al. (2007). Using IRAF, we removed latent charge in the IRS images row-by-row by fitting the linear background increase over time. Subsequently, we masked "rogue" pixels using the IDL routine IRSCLEAN. After cleaning, we constructed sky images for each target position using the five other pointings from the same mapping AOR. The resulting sky images were subtracted from the corresponding science frames, and the differences were then co-added to produce a final 2D spectrum at each position. We extracted 1D spectra using the SPICE package provided by the Spitzer Science Center, using optimal extraction. We used an extraction aperture half the default size in order to avoid contamination from other sources (see below), but we corrected to full-aperture fluxes using observations of standard stars.

For J0901, extraction of the 1D spectra was complicated by an interloping source, SDSS J090125.59+181427.8 (see Figure 1a), lying $\sim 46''$ away from the lens. From its IRS spectrum, this object is likely to be a quasar at $z \sim 1.3$, in agreement with the assessment of its optical colors by Richards et al. (2009). Its spectrum in one pointing often lay on or near the position of a J0901 spectrum in *another* pointing; combined with the fact that J0901 itself is bright and extended, this situation meant that a given "sky" frame included the true background, light from the interloping source, and residual flux from J0901 at other map positions, leading to oversubtraction in our final 2D spectra (e.g., Figure 1a). To correct for this effect, we extracted 1D spectra of the negative sky echoes at *different* locations in the 2D spectrum whose combination should have experienced the *same* oversubtraction as the position in question (e.g., Figure 1b). By combining such measurements, we constructed an empirical model for the oversubtraction of each of our target spectra that accounted for both continuum and PAH features. We found that the correction was fairly mild, leading to a $\sim 10 - 25\%$ flux increase over the uncorrected spectrum.

As an alternative to the above procedure, we tried to create sky images using only dithers whose positions were far enough away that no oversubtraction occurred. Doing so meant constructing sky images from many fewer frames, often from only one or two other positions. As a result, we found the reduced (cleaned and sigma-clipped) 2D spectra were affected by rogue pixels whose effects would otherwise have been eliminated. Such pixels not only increased the uncertainty in our final 1D spectrum, but also introduced small-scale

features that do not correspond with any known emission features. Given the undesirable effects of this approach to sky subtraction, we opted for the method described above, which uses all of the original frames. We note that the spectra produced via our two sky subtraction procedures yield similar flux densities within the measurement uncertainties.

For both J1206 and J0901, the error spectrum at each position was calculated using SPICE and standard deviation frames constructed in IRAF. The final error spectrum is that of all the positions added in quadrature. For J0901, we include an additional systematic uncertainty associated with our sky correction, raising the final error spectrum by a factor $\sim \sqrt{2}$.

3. Results

3.1. SDSS J120602.09+514229.5

Figure 2a shows the extracted IRS spectra for J1206. On top of a rising continuum, prominent PAH features are present at 6.2, 7.7, and 11.3 μm. In addition, a strong [S IV] feature is present at 10.5 μm. In order to compare the spectrum to those of local starbursting analogs, we fit template *Infrared Space Observatory* spectra of 30 Doradus, Circinus, M82, NGC 253, and NGC 1068 from Sturm et al. (2000), and the average *Spitzer* starburst template from Brandl et al. (2006). For the fit we allow a varying contribution from the templates as well as an additional power law continuum (normalized to 6.2 μm): $F_{\nu,\mathrm{fit}} = C_1 \times [\mathrm{Template}] + C_2 \times (\lambda/6.2\,\mu\mathrm{m})^{\alpha}$, where C_1 is dimensionless and C_2 has units of mJy. The three parameters for the fit were sampled using a standard Metropolis-Hastings MCMC (Markov chain Monte Carlo) algorithm. Figure 2b shows two of the template spectra that provide good fits. Table 1 shows the inferred median, 68% confidence limits, and best-fit parameters for the templates that provided reasonable fits. We find that the spectrum is well fit by the M82 template ($\chi^2_{\mathrm{red}} = 0.96$), and marginally fit by the NGC 253 and average starburst templates ($\chi^2_{\mathrm{red}} = 1.20, 1.14$). In contrast, the other templates from Sturm et al. (for 30 Doradus, Circinus, and NGC 1068) fit the spectrum poorly ($\chi^2_{\mathrm{red}} > 10$) due to the lack of strong PAH features. For each of the acceptable templates, the best fit includes an additional, steeply-rising continuum with a power law index of $\alpha \sim 3.3$.

Exploiting the similarity to the spectrum of M82, we can estimate the far-IR luminosity

of J1206 as

$$L_{\rm FIR}({\rm J1206}) = L_{\rm FIR}({\rm M82}) \cdot \left(\frac{D_L({\rm J1206})}{D({\rm M82})}\right)^2 \cdot \frac{1}{\mathcal{M}} \cdot \frac{S_{\nu'}({\rm J1206})\,\Delta\nu'}{S_\nu({\rm M82})\,\Delta\nu} \quad (1)$$

$$= 2.76 \times 10^{16}\,L_\odot \cdot \frac{S_{\nu'}({\rm Clone})\,\Delta\nu'}{S_\nu({\rm M82})\,\Delta\nu} \quad (2)$$

in terms of the distance to M82 (3.63 Mpc: Freedman et al. 2001) and the corresponding $40-400\,\mu$m far-IR luminosity ($4.1\times10^{10}\,L_\odot$: Sanders et al. 2003), the magnification of J1206 ($\mathcal{M} = 27 \pm 1$: Lin et al. 2009), and the luminosity distance to J1206 for a $(h, \Omega_m, \Omega_\Lambda) = (0.7, 0.3, 0.7)$ cosmology. The remaining term in Equation 2 is the ratio of the observed spectra in flux density units after corresponding rest-frequency channels ($\Delta\nu$ and $\Delta\nu' = \Delta\nu/(1+z)$) are matched up. This is precisely the value of C_1 delivered by our template fitting, leading to an estimate of $L_{\rm FIR} = 2.4\times10^{11}\,L_\odot$ that places J1206 in the LIRG regime. In estimating $L_{\rm FIR}$ we ignore the additional power-law component used in template fitting, since its contribution should be negligible at far-IR wavelengths.

To extract and interpret the features of the spectrum, we have also computed a fit using the Drude profiles defined in Draine & Li (2007) for PAH features, Gaussian line profiles for ionized species expected to be strong, and a simple power law continuum ($\propto \lambda^\alpha$). In addition, the fit includes extinction effects from 9.7 μm silicate absorption. The results of this fit are plotted in Figure 2c and tabulated in Table 2. To assess the strength of the PAH emission, we compare the rest-frame equivalent widths (EWs) of the 6.2, 7.7 ($\equiv$ 7.41+7.61+7.85), and 11.3 ($\equiv 11.23 + 11.33$) μm PAH features to those of local starbursting systems. Comparisons of EWs are known to be sensitive to the details of how authors define the underlying continuum. In particular, continuum levels are often defined by the values of the data seen on either side of emission features (see e.g., Brandl et al. 2006; Pope et al. 2008). Such definitions result in systematically higher continua and lower PAH EWs than found by comprehensive fits to the spectra (e.g., Siana et al. 2009). To facilitate interpretation of the EW values reported in Table 2, we analyze the average starburst spectrum of Brandl et al. (2006) using the same conventions as for J1206. We find EWs for the average starburst spectrum that are factors $\sim 1-8$ higher than derived by Brandl et al. (2006) for their own data. Nevertheless, this approach provides a consistent way of measuring and comparing EW values to our data. Relative to the average starburst spectrum, J1206 has EWs that are lower by factors of 1.2, 1.5, and 1.2 for the 6.2, 7.7, and 11.3 μm PAH features, respectively. This slight deficiency is not surprising, given the additional power-law continuum preferred by our template fitting above.

The two most striking features of the $\sim 4.5-12\,\mu$m spectrum of J1206 are its steep underlying continuum and prominent [S IV] emission. In high-resolution studies of local star-forming galaxies, the latter line is fairly common and appears weakly in starbursts

(Bernard-Salas et al. 2009) and ULIRGs (Farrah et al. 2007), but is much stronger in blue compact dwarfs (BCDs; Hao et al. 2009). At lower resolution this line is unresolved, and only the strongest emitters are detected (see, e.g., Brandl et al. 2006; Wu et al. 2006). Comparing the relative strengths of [S IV] and PAH emission of J1206 to those of local counterparts, we identify the two low-resolution mid-IR spectra of the starburst NGC 1222 (Brandl et al. 2006) and the BCD UGC 4274 (Wu et al. 2006) as close analogs.

Using the optical spectroscopy of Liu & Kennicutt (1995) for NGC 1222 and Ho et al. (1997) for UGC 4274, we calculate the oxygen abundance in each galaxy using the $N2$ and $O3N2$ indicators calibrated by Pettini & Pagel (2004). We find $12+\log(\mathrm{O/H})_{\mathrm{N2}} = 8.48, 8.43$ and $12+\log(\mathrm{O/H})_{\mathrm{O3N2}} = 8.38, 8.37$ for NGC 1222 and UGC 4274, respectively. For J1206, Hainline et al. (2009) use near-IR spectroscopy to find $12+\log(\mathrm{O/H})_{\mathrm{N2}} = 8.50 \pm 0.18$ and $12+\log(\mathrm{O/H})_{\mathrm{O3N2}} = 8.34 \pm 0.14$, in good agreement with the putative local counterparts. Given the consistency between the spectra and the oxygen abundances, modulo a factor ~ 2.5 uncertainty in the calibration of the optical diagnostics (Pettini & Pagel 2004), we conclude that NGC 1222 and UGC 4274 have physical conditions similar to those of J1206.

In addition to oxygen abundances, we can consider the ratios of ionized sulfur and neon lines [S IV] $10.5\,\mu$m/[S III] $18.7\,\mu$m and [Ne III] $15.6\,\mu$m/[Ne II] $12.8\,\mu$m for NGC 1222 and UGC 4274. These quantities are well-known proxies for the hardness of the radiation field (see Figure 9 of Hao et al. 2009), which is also a function of metallicity (Wu et al. 2006). The galaxies have similar ratios of [Ne III]/[Ne II] ~ 1.30 and [S IV]/[S III] ~ 0.35, and lie between lower excitation starbursts and higher excitation BCDs on a [S IV]/[S III] versus [Ne III]/[Ne II] excitation diagram (Hao et al. 2009), implying a moderately hard radiation field. Using stellar models, Thornley et al. (2000) estimate the hardness of the radiation in starbursts by relating [Ne III]/[Ne II] to the ratio of the infrared and Lyman continuum luminosities ($L_{\mathrm{IR}}/L_{\mathrm{Lyc}}$). Since NGC 1222 and UGC 4274 have higher [Ne III]/[Ne II] ratios than the Thornley et al. sample, we extrapolate their results and find $3 \lesssim L_{\mathrm{IR}}/L_{\mathrm{Lyc}} \lesssim 20$ indicating a somewhat lower range than for their more typical starbursts ($4 \lesssim L_{\mathrm{IR}}/L_{\mathrm{Lyc}} \lesssim 30$). If present in J1206, such hard radiation would cause significant heating of small dust grains and naturally explain the steep continuum in our IRS spectrum. Unfortunately, [Ne III], [Ne II], and [S III] all lie outside of our spectral coverage, preventing definitive confirmation of this hypothesis.

In J1206, the apparent consistency between metallicity estimates based on rest-frame optical and (via analogy with NGC 1222 and UGC 4274) infrared observations suggests that we are not seeing discrepancies of the sort seen in the most violent local mergers. For ULIRGs, abundances derived from optical line diagnostics (even after careful extinction corrections) are lower than those derived from mid-infrared spectra, likely because the former

are depressed by inflows of metal-poor gas from the outskirts of progenitor disks (Rupke et al. 2008) while the latter reflect rapid local enrichment in the most deeply embedded star-forming regions (Veilleux et al. 2009). Metallicities for J1206 appear internally consistent across both obscured and unobscured regions, suggesting a less traumatic recent history that is consistent with the system's relatively modest far-IR luminosity.

Our conclusions about the implied metallicity and excitation state of J1206 require a certain degree of caution. While in good agreement with optical measurements, our selection of local infrared analogs for J1206 is based mostly on our detection of a single line, [S IV], whose correlations with PAH strength, metallicity, and spectral hardness may be uncertain by 30% or more (Wu et al. 2006; Hao et al. 2009; Hunt et al. 2010). Further, metallicities derived from the optical emission lines in NGC 1222 and UGC 4274 are themselves uncertain by a factor ~ 2.5 (Pettini & Pagel 2004). Nevertheless, the consistency (within the measured uncertainties) between the IR spectra of J1206, NGC 1222, and UGC 4274, as well as the optical and IR properties of NGC 1222 and UGC 4274, is encouraging, indicating that the three objects do manifest similar physical conditions. In the future, more robust estimates of the metallicity and excitation properties of J1206 will be possible with measurements of additional emission lines over a wider spectral range.

We can also consider the absence of other emission lines in our IRS spectrum, which shows no significant ionic or molecular features other than [S IV]. In Table 2, we report 3σ upper limits on [Ar II] at $6.99\,\mu$m, [Ar III] at $8.99\,\mu$m, and [Ne VI] at $7.65\,\mu$m. At first glance, it seems surprising we do not detect [Ar II], given that it is commonly detected in starburst systems (Brandl et al. 2006), including M82 and NGC 253. As discussed above, however, the presence of a rising continuum and [S IV] emission imply higher excitation in J1206 than in average starbursting systems. Given that the ionization potential of [S IV] at 34.8 eV is a factor ~ 2 greater than [Ar II] at 15.8 eV, [Ar II] is likely weak because most of the argon is more highly ionized. This effect is seen in BCD galaxies, which are known to exhibit high excitation states (Hao et al. 2009; Hunt et al. 2010). As a consistency check, we note that our upper limit for [Ar III] (ionization potential: 27.6 eV) implies a ratio of [Ar III]/[S IV] that is consistent with values seen in local starbursts and BCDs (Brandl et al. 2006; Wu et al. 2006).

In principle, an alternative explanation for the steep continuum and [S IV] emission in J1206 is the presence of an AGN. Indeed, Seyfert 2 galaxies are known to show PAH and [S IV] features, and exhibit strong, rising continua due to heating of small dust grains. To address this concern, we consider the diagnostics of Laurent et al. (2000) to disentangle starburst vs. AGN energetics. Specifically, we use the flux ratio of $6.2\,\mu$m PAH to $5.1-6.8\,\mu$m continuum, which is lower (higher) for a larger (smaller) AGN contribution to the infrared

luminosity. For J1206, this ratio is 0.66 ± 0.08, much larger than the $\lesssim 0.3$ values of AGN-dominated galaxies like NGC 1068 and similar to results for PDR-dominated systems like M82 and NGC 520, which have $\lesssim 5\%$ of the emission contributed by an AGN (see Figures 5 and 6 in Laurent et al.). Reinforcing this conclusion, Seyferts with similar [S IV] and [Ar II] strengths have 6.2 μm PAH EWs that are $> 2\sigma$ lower than for J1206 (Gallimore et al. 2010).[1] Finally, J1206 has a ratio [Ne VI]/[S IV]< 0.38 (3σ), which is lower than that in any Seyfert for which [S IV] is detected (Sturm et al. 2002). We conclude that nuclear activity plays little role in the mid-IR spectrum of J1206.

3.2. SDSS J090122.37+181432.3

Using the reduction procedure outlined in Section 2, we have derived the final rest-frame spectrum for J0901 that is shown in Figure 3a. Following the same procedure as above, we fit the same starburst templates to the spectrum as in Section 3.1, with the results shown in Table 1. As for J1206, we find that the spectrum is best fit by a scaled version of M82 ($\chi^2_{\rm red} = 0.95$), less well by NGC 253 or the average starburst template of Brandl et al. (2006) ($\chi^2_{\rm red} = 1.42, 1.26$, respectively), and poorly by the other Sturm et al. templates ($\chi^2_{\rm red} > 20$). For the NGC 253 and average starburst fits, the higher χ^2 values originate from the enhanced 9.7 μm silicate absorption in J0901, which is not seen in the templates (see Figure 3b). In contrast to J1206, J0901 exhibits only weak evidence for additional power-law emission, with fits favoring a component that is negligible or has highly uncertain parameters. Again (as in Section 3.1) exploiting the similarity to the spectrum of M82, and adopting a lens magnification of $\mathcal{M} \approx 8$ (A. West et al. 2010, in preparation), we estimate its intrinsic far-IR luminosity to be $3.8 \times 10^{12}\,L_\odot$, placing it in the ULIRG regime.

As for J1206, we simultaneously fit the spectrum with a combination of continuum and relevant PAH features and atomic emission lines. We find the degree of inferred silicate absorption is degenerate with the contributions of weak PAH emission features to the spectrum. In general, this degeneracy has little effect on the inferred PAH emission, except in the relative contributions of the 11.23 and 11.33 μm lines to the 11.3 μm PAH feature. In fact, the 6.2 μm and blended 7.7 μm and 11.3 μm PAH strengths are essentially unaffected. Ultimately, we have opted to use solutions with higher silicate extinction, in agreement with the template fits above. We present the results of this fit in Table 2 and plot the results in

[1] While such comparisons involve difficulties in continuum definitions (see above), we note that Laurent et al. and Gallimore et al. also use comprehensive fits of all relevant mid-IR features to derive their continua, and therefore should have results similar to ours.

Figure 3c.

The PAH emission in J0901 is strong relative to local starbursts, with EWs of each feature that are a factor $\sim 1.6 - 1.9$ times larger than the Brandl et al. (2006) average values. The strengths of the 6.2, 7.7, and 11.3 μm PAH features serve as common diagnostics of the driving mechanism(s) for infrared emission in infrared-luminous galaxies (e.g., Roche et al. 1991; Genzel et al. 1998; Laurent et al. 2000; Imanishi et al. 2007; Veilleux et al. 2009; Baum et al. 2010; Gallimore et al. 2010). In particular, suppressed PAH emission (especially at shorter wavelengths) is indicative of a significant AGN contribution to the bolometric infrared luminosity. Given the strength of the observed PAH emission, coupled with the shallow continuum, we conclude that accretion plays a small role in the mid-IR properties of J0901. However, Hainline et al. (2009) examined the optical emission line ratios and found values of [O III]/Hβ and [N II]/Hα indicative of an AGN, consistent with the significant [N V] and weak [Si IV] and [C IV] emission seen in the object's rest-UV spectrum (Diehl et al. 2009).

To assess this apparent contradiction, we consider the expected flux contribution to our mid-IR spectrum by an AGN whose optical properties resemble those of J0901. Specifically, we treat [O III] 5007 Å emission as a proxy for AGN strength and scale the *ISO* template of NGC 1068 by the factor required to reduce the integrated [O III] flux of NGC 1068 (Moustakas & Kennicutt 2006) to the Hainline et al. value. The dotted line in Figure 3c shows the corresponding contribution of the scaled NGC 1068 spectrum: roughly 57% and 35% of the continuum flux at 5 and 10 μm, respectively. This comparison demonstrates that reliance on rest-frame UV/optical measurements alone may provide a bolometrically unrepresentative picture of the physical properties of high-redshift systems.

Finally, we examine our IRS spectrum of J0901 for ionic and molecular emission. Here J0901 is quite unlike J1206, showing [Ar II] but no [S IV] emission. The EW of [Ar II] is similar to that in the average starburst spectrum of Brandl et al. (2006) (see Figure 3b). As discussed above, [Ar II] is weaker for systems with high-excitation interstellar media. Therefore, J0901 must be bathed in a softer radiation field than J1206, reinforcing the conclusion that AGN emission plays little role in the IR properties of the system. With our upper limit on [Ar III] we find [Ar III]/[Ar II]< 0.83, which when combined with the argon excitation versus abundance relation from Verma et al. (2003) implies an abundance ratio of [Ar/H] $\gtrsim 1.3$. Assuming that argon abundance is a reliable tracer of the global metallicity, this implies $Z \gtrsim 1.3\, Z_\odot$ for J0901. While an intriguing result, we recommend caution in interpreting it given the large uncertainty (factor ~ 2) in the Verma et al. relation and its reliance on a single ionic line whose measurement uncertainties are $\sim 25\%$.

4. Conclusions

We have obtained *Spitzer*/IRS spectra of two $z \sim 2$ UV-bright star-forming galaxies, that are magnified by strong gravitational lensing. At rest wavelengths of $\sim 5 - 12\,\mu$m, the spectra reveal strong PAH emission at 6.2, 7.7, and 11.3 μm, indicating that these objects are undergoing intense star formation. The strength of the PAH emission implies these objects have properties in line with those of local starbursting galaxies. We find this similarity to local starburst galaxies is confirmed by our empirical template fits, in which both galaxies are well fit by simple, rescaled versions of M82. In detail, however, analysis of PAH strengths and emission line and continuum diagnostics reveals disparate properties. We summarize our conclusions as follows:

1. In J1206, we find PAH EWs lower than those in the local starburst spectrum of Brandl et al. (2006), due to an enhanced power-law continuum. In contrast, J0901 exhibits PAH EWs that are factors 1.6–1.9 times larger than the local average.

2. We detect significant [S IV] emission in J1206. By analogy with two local galaxies with similar mid-IR spectra, NGC 1222 and UGC 4274, we infer a sub-solar metallicities of $\sim 0.5\,Z_\odot$, in agreement with the published optical measurement (Hainline et al. 2009). The consistency of the optical and infrared metallicity estimates suggests J1206 has not undergone a recent violent merger. Considering the [S IV]/[S III] and [Ne III]/[Ne II] ratios of the local objects, we argue that J1206 is characterized by a moderately hard radiation field, which naturally explains the steeply rising continuum and lack of [Ar II] emission.

3. In J0901, we detect strong PAH emission but no [S IV] or significant rising continuum. These results indicate that the mid-IR properties of J0901 are consistent with purely starburst-driven energetics. This inference contrasts with the implications of optical spectroscopy, where emission line ratios show the presence of an AGN; however, scaling from the [O III] flux of a local AGN implies the AGN contributes $< 57\%$ of the mid-IR continuum. Thus, from its rest-frame UV through IR properties, J0901 likely hosts a narrow-line AGN whose IR emission is overwhelmed by that of its surrounding starburst. This analysis highlights the need for future IR studies of high-redshift objects if we are to determine their physical properties robustly.

4. With the detection of [Ar II], we are able to put an upper limit on the metallicity of J0901. Using the argon abundance and excitation relation of Verma et al. (2003), we find $Z \gtrsim 1.3\,Z_\odot$, similar to many local starbursts.

We thank Eckhard Sturm for providing template spectra of local galaxies in electronic form, and Anderson West and Tom Diehl for sharing the results of their lens modelling. This work is based on observations made with the *Spitzer Space Telescope*, which is operated by the Jet Propulsion Laboratory, California Institute of Technology under a contract with NASA. Support for this work was provided by NASA through two awards issued by JPL/Caltech.

REFERENCES

Adelberger, K. L., Steidel, C. C., Shapley, A. E., Hunt, M. P., Erb, D. K., Reddy, N. A., & Pettini, M. 2004, ApJ, 607, 226

Allam, S. S., Tucker, D. L., Lin, H., Diehl, H. T., Annis, J., Buckley-Geer, E. J., & Frieman, J. A. 2007, ApJ, 662, L51

Baum, S. A., et al. 2010, ApJ, 710, 289

Belokurov, V., et al. 2007, ApJ, 671, L9

Bernard-Salas, J., et al. 2009, ApJS, 184, 230

Brandl, B. R., et al. 2006, ApJ, 653, 1129

Diehl, H. T., et al. 2009, ApJ, 707, 686

Draine, B. T., & Li, A. 2007, ApJ, 657, 810

Farrah, D., et al. 2007, ApJ, 667, 149

Freedman, W. L., et al. 2001, ApJ, 553, 47

Gallimore, J. F., et al. 2010, ApJS, 187, 172

Genzel, R., et al. 1998, ApJ, 498, 579

Hainline, K. N., Shapley, A. E., Kornei, K. A., Pettini, M., Buckley-Geer, E., Allam, S. S., & Tucker, D. L. 2009, ApJ, 701, 52

Hao, L., Wu, Y., Charmandaris, V., Spoon, H. W. W., Bernard-Salas, J., Devost, D., Lebouteiller, V., & Houck, J. R. 2009, ApJ, 704, 1159

Hennawi, J. F., et al. 2008, AJ, 135, 664

Ho, L. C., Filippenko, A. V., Sargent, W. L. W., & Peng, C. Y. 1997, ApJS, 112, 391

Houck, J. R., et al. 2004, ApJS, 154, 18

Hunt, L. K., Thuan, T. X., Izotov, Y. I., & Sauvage, M. 2010, ApJ, 712, 164

Imanishi, M., Dudley, C. C., Maiolino, R., Maloney, P. R., Nakagawa, T., & Risaliti, G. 2007, ApJS, 171, 72

Kubo, J. M., Allam, S. S., Annis, J., Buckley-Geer, E. J., Diehl, H. T., Kubik, D., Lin, H., & Tucker, D. 2009, ApJ, 696, L61

Laurent, O., Mirabel, I. F., Charmandaris, V., Gallais, P., Madden, S. C., Sauvage, M., Vigroux, L., & Cesarsky, C. 2000, A&A, 359, 887

Lehnert, M. D., & Bremer, M. 2003, ApJ, 593, 630

Lin, H., et al. 2009, ApJ, 699, 1242

Liu, C. T., & Kennicutt, Jr., R. C. 1995, ApJ, 450, 547

Lutz, D., Valiante, E., Sturm, E., Genzel, R., Tacconi, L. J., Lehnert, M. D., Sternberg, A., & Baker, A. J. 2005, ApJ, 625, L83

Menéndez-Delmestre, K., et al. 2009, ApJ, 699, 667

Moustakas, J., & Kennicutt, Jr., R. C. 2006, ApJS, 164, 81

Pettini, M., & Pagel, B. E. J. 2004, MNRAS, 348, L59

Pope, A., et al. 2008, ApJ, 675, 1171

Reddy, N. A., & Steidel, C. C. 2004, ApJ, 603, L13

Reddy, N. A., Steidel, C. C., Erb, D. K., Shapley, A. E., & Pettini, M. 2006a, ApJ, 653, 1004

Reddy, N. A., Steidel, C. C., Fadda, D., Yan, L., Pettini, M., Shapley, A. E., Erb, D. K., & Adelberger, K. L. 2006b, ApJ, 644, 792

Reddy, N. A., Steidel, C. C., Pettini, M., Adelberger, K. L., Shapley, A. E., Erb, D. K., & Dickinson, M. 2008, ApJS, 175, 48

Reddy, N. A., Erb, D. K., Pettini, M., Steidel, C. C., & Shapley, A. E. 2010, ApJ, 712, 1070

Richards, G. T., et al. 2009, ApJS, 180, 67

Roche, P. F., Aitken, D. K., Smith, C. H., & Ward, M. J. 1991, MNRAS, 248, 606

Rupke, D. S. N., Veilleux, S., & Baker, A. J. 2008, ApJ, 674, 172

Sanders, D. B., Mazzarella, J. M., Kim, D.-C., Surace, J. A., & Soifer, B. T. 2003, AJ, 126, 1607

Shin, M., Strauss, M. A., Oguri, M., Inada, N., Falco, E. E., Broadhurst, T., & Gunn, J. E. 2008, AJ, 136, 44

Siana, B., Teplitz, H. I., Chary, R., Colbert, J., & Frayer, D. T. 2008, ApJ, 689, 59

Siana, B., et al. 2009, ApJ, 698, 1273

Smail, I., et al. 2007, ApJ, 654, L33

Steidel, C. C., Adelberger, K. L., Giavalisco, M., Dickinson, M., & Pettini, M. 1999, ApJ, 519, 1

Steidel, C. C., Adelberger, K. L., Shapley, A. E., Pettini, M., Dickinson, M., & Giavalisco, M. 2003, ApJ, 592, 728

Steidel, C. C., Giavalisco, M., Dickinson, M., & Adelberger, K. L. 1996, AJ, 112, 352

Sturm, E., Lutz, D., Tran, D., Feuchtgruber, H., Genzel, R., Kunze, D., Moorwood, A. F. M., & Thornley, M. D. 2000, A&A, 358, 481

Sturm, E., Lutz, D., Verma, A., Netzer, H., Sternberg, A., Moorwood, A. F. M., Oliva, E., & Genzel, R. 2002, A&A, 393, 821

Teplitz, H. I., et al. 2007, ApJ, 659, 941

Thornley, M. D., Schreiber, N. M. F., Lutz, D., Genzel, R., Spoon, H. W. W., Kunze, D., & Sternberg, A. 2000, ApJ, 539, 641

Valiante, E., Lutz, D., Sturm, E., Genzel, R., Tacconi, L. J., Lehnert, M. D., & Baker, A. J. 2007, ApJ, 660, 1060

Veilleux, S., et al. 2009, ApJS, 182, 628

Verma, A., Lutz, D., Sturm, E., Sternberg, A., Genzel, R., & Vacca, W. 2003, A&A, 403, 829

Weedman, D. W., Le Floc'h, E., Higdon, S. J. U., Higdon, J. L., & Houck, J. R. 2006, ApJ, 638, 613

Wu, Y., Charmandaris, V., Hao, L., Brandl, B. R., Bernard-Salas, J., Spoon, H. W. W., & Houck, J. R. 2006, ApJ, 639, 157

Yan, L., et al. 2007, ApJ, 658, 778

Yee, H. K. C., Ellingson, E., Bechtold, J., Carlberg, R. G., & Cuillandre, J. 1996, AJ, 111, 1783

This preprint was prepared with the AAS LaTeX macros v5.2.

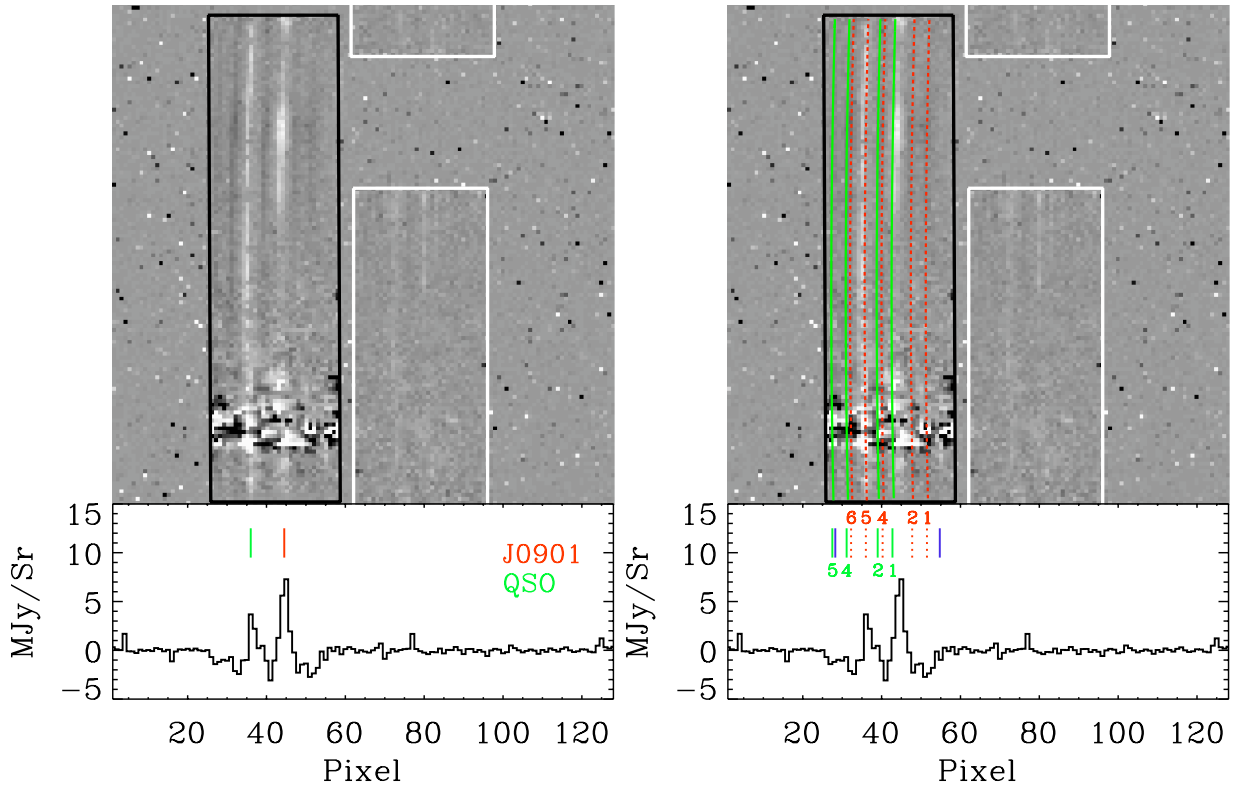

Fig. 1.— (a) Left: reduced 2D spectrum for J0901 at our third map position, after subtraction of a model for the sky. The black and white rectangles indicate the areas of the array exposed to the spectrometer for LL1 and LL2, respectively, with wavelength increasing downward. Two LL1 spectra are visible: the detection on the right is our target J0901, while on the left is the interloping source SDSS J090125.59+181427.8. From the pattern of the neighboring pixels, it is clear that the background is oversubtracted due to the relatively bright spectra of J0901 and the additional source. Plotted below the spectrum are the data for the row corresponding to the peak of the J0901 spectrum, where the oversubtraction is the worst. (b) Right: same data overplotted with the positions of the two spectra for the other map positions, indicated by the numbers in the lower panel. The dotted red lines mark the positions of the J0901 spectra, while the solid green lines mark those of the additional source. For this (i.e., the third) map position, the spectrum for J0901 lies just next to the rightmost solid green line (the position of the interloping source for our first map position) and between two dashed red lines (the positions of J0901 for our second and fourth map positions). To correct for this effect, we measure the sky at appropriate positions, indicated by the blue line segments. The combination of these measurements gives an accurate model for the oversubtraction, which is then added to the data.

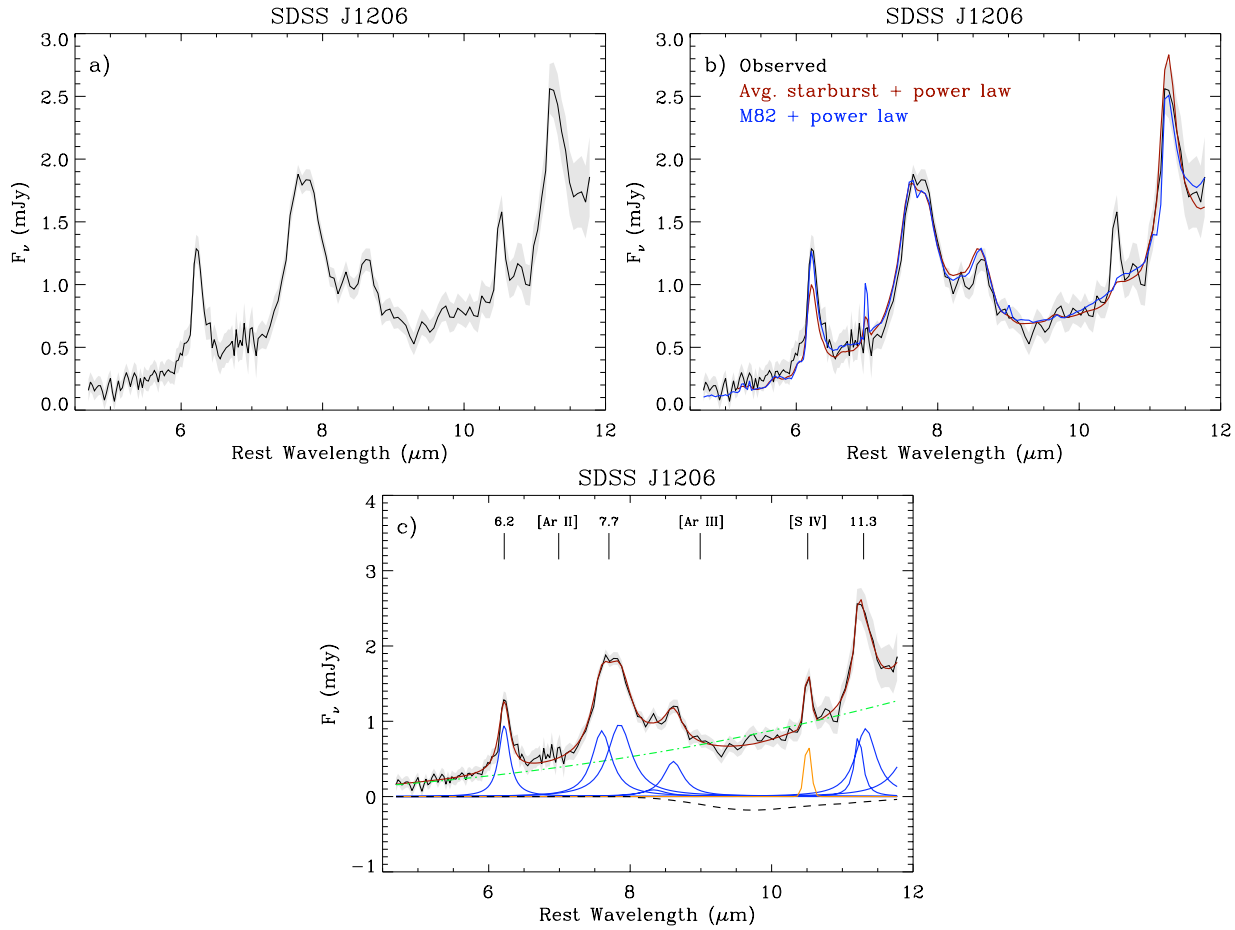

Fig. 2.— (a) IRS spectrum of J1206. The observed spectrum is plotted in black after redshifting to rest wavelength for $z = 2.00$. The light grey band corresponds to the 1σ uncertainty associated with the spectrum. (b) Plotted in blue and red, respectively, are the best fit template + power law spectra (see text) for M82 and the average starburst spectrum of Brandl et al. (2006) for the parameters listed in Table 1. (c) A comprehensive fit (red) to the spectrum using Drude profiles for PAH features (blue), Gaussian profiles for ionic lines (orange), and a power law continuum (green dot dashed). The fit also includes 9.7 μm silicate extinction (black dashed).

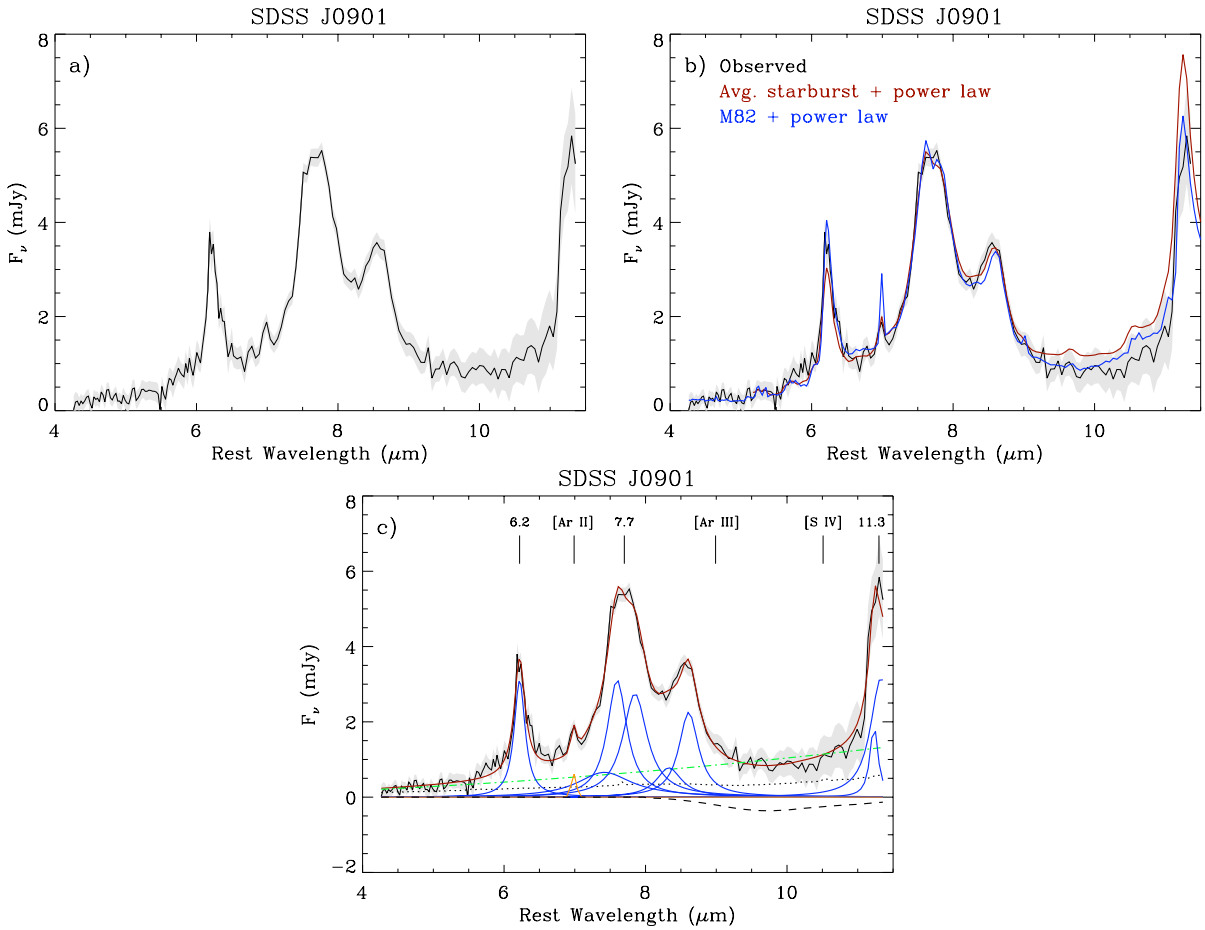

Fig. 3.— (a) Observed IRS spectrum of J0901 plotted in black after redshifting to rest wavelength for $z = 2.26$. (b) Template + power law fits to the spectrum, with notation as in Figure 2b. (c) Comprehensive fit, with notation as in Figure 2c. The additional dotted line indicates the AGN contribution to the spectrum implied by rest-frame optical measurements (see Section 3.2).

Table 1. Local starburst template fits.

Template	$\log(C_1)$	$\log(C_2/\mathrm{mJy})$	α	Fit type
		J1206		
M82	$-5.063^{+0.006}_{-0.004}$	$-0.78^{+0.11}_{-0.16}$	$3.3^{+0.2}_{-0.2}$	MCMC results
	-5.06	-0.84	3.1	Best Fit: $\chi^2_{\rm red} = 0.96$
NGC 253	$-4.938^{+0.128}_{-0.102}$	$-0.79^{+0.12}_{-0.14}$	$3.2^{+0.2}_{-0.2}$	MCMC results
	-5.03	-0.86	3.0	Best Fit: $\chi^2_{\rm red} = 1.20$
Avg. Starburst	$-2.960^{+0.051}_{-0.051}$	$-0.55^{+0.12}_{-0.22}$	$3.3^{+0.2}_{-0.2}$	MCMC results
	-2.99	-0.72	3.1	Best Fit: $\chi^2_{\rm red} = 1.14$
		J0901		
M82	$-4.557^{+0.061}_{-0.042}$	$-1.08^{+0.22}_{-0.16}$	$3.1^{+2.2}_{-2.1}$	MCMC results
	-4.52	-1.10	2.6	Best Fit: $\chi^2_{\rm red} = 0.95$
NGC 253	$-4.675^{+0.045}_{-0.058}$	$-0.69^{+0.13}_{-0.18}$	$3.2^{+0.8}_{-0.6}$	MCMC results
	-4.62	-0.56	3.6	Best Fit: $\chi^2_{\rm red} = 1.42$
Avg. Starburst	$-2.453^{+0.038}_{-0.035}$	$-6.51^{+0.18}_{-0.17}$	$0.6^{+0.1}_{-0.1}$	MCMC results
	-2.46	-6.42	0.5	Best Fit: $\chi^2_{\rm red} = 1.26$

Note. — $F_{\nu,\rm fit} = C_1 \times [\mathrm{Template}] + C_2 \times (\lambda/6.2\,\mu\mathrm{m})^{\alpha}$. Right-hand column indicates fit type for a given row. "MCMC results" report the median and 68% confidence intervals, inferred using a Monte Carlo Markov Chain method. "Best Fit" values correspond to the highest likelihood fit, derived using optimization techniques.

Table 2. Derived feature strengths.

	J1206		J0901	
Wavelength	Observed Flux	Rest EW	Observed Flux	Rest EW
μm	10^{-15} erg s^{-1} cm^{-2}	μm	10^{-15} erg s^{-2} cm^{-1}	μm
6.22 PAH	21.7 (1.2)	1.12	70.2 (3.1)	2.12
6.99 [Ar II]	< 1.9	< 0.12	3.5 (0.9)	0.11
7.42 PAH	–	–	52.0 (10.8)	1.59
7.60 PAH	24.2 (1.6)	1.21	84.7 (4.5)	2.61
7.65 [Ne VI]	< 0.8	< 0.10	< 2.6	< 0.08
7.85 PAH	30.9 (1.8)	1.55	87.0 (4.1)	2.70
8.33 PAH	3.1 (1.6)	0.20	22.8 (3.9)	0.71
8.61 PAH	10.2 (1.2)	0.51	47.9 (2.9)	1.51
8.99 [Ar III]	< 2.8	< 0.05	< 2.9	< 0.09
10.51 [S IV]	2.1 (0.1)	0.10	< 4.8	< 0.15
11.23 PAH	3.7 (1.3)	0.19	9.6 (6.6)	0.31
11.33 PAH	13.2 (3.4)	0.61	42.1 (15.4)	1.37
11.99 PAH	3.2 (1.4)	0.78	–	–

Note. — Equivalent width values are based on the green dot dashed lines (power-law continuum fits) in Figures 2c and 3c. Upper limits are based on 3σ uncertainties in the spectra.